CO_2-induced single-crystal to single-crystal transformations of an interpenetrated flexible MOF explained by *in situ* crystallographic analysis and molecular modeling

Arpan Hazra, Dewald P. van Heerden, Somananda Sanyal, Prem Lama, Catharine Esterhuysen and Leonard J. Barbour*

Department of Chemistry and Polymer Science, University of Stellenbosch, Matieland, 7600, South Africa. E-mail: ljb@sun.ac.za; Fax: (+27) 21-808-3360

Supporting information contents

Preparation of $\mathbf{1}_{cp}$, $[Zn_2(ndc)_2(bpa)]_n$

To a 10 mL autoclave were added $Zn(NO_3)_2 \cdot 6H_2O$ (30 mg, 0.1 mmol), H_2ndc (22 mg, 0.1 mmol), bpa (18 mg, 0.1 mmol) and 3 mL of H_2O (H_2ndc = 1,4-naphthalene dicarboxylic acid and bpa = 1,2-bis-(4-pyridyl)ethane). The tube was sealed and heated in an oven to 180 °C for 3 days, and then cooled to ambient temperature at the rate of 5 °C h^{-1} to form colourless blocks of $\mathbf{1}_{cp}$, which were washed with water–ethanol and dried in air. Yield: 28 mg (72% yield based on Zn).

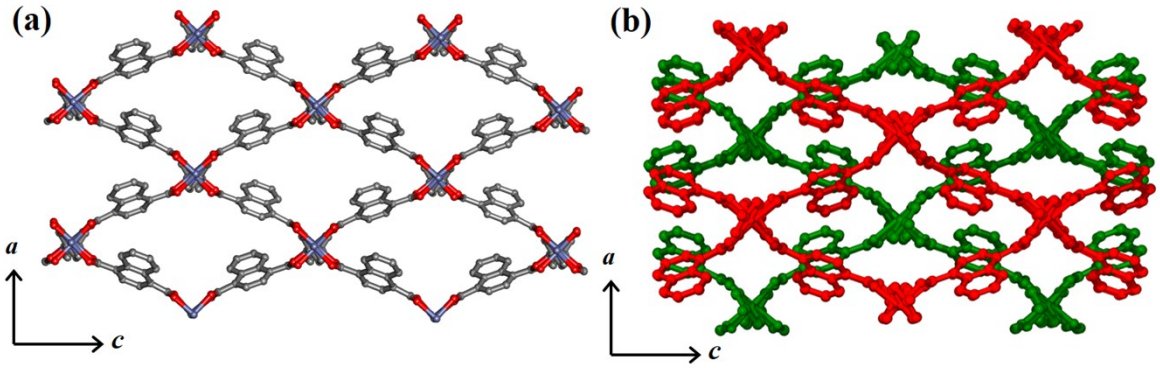

Fig. S1: (a) 2D rhombic grid formed by ndc and the paddle-wheel SBU in $\mathbf{1}_{cp}$. (b) view of twofold entanglement in this framework. Hydrogen atoms are omitted and only one disordered orientation is shown for clarity.

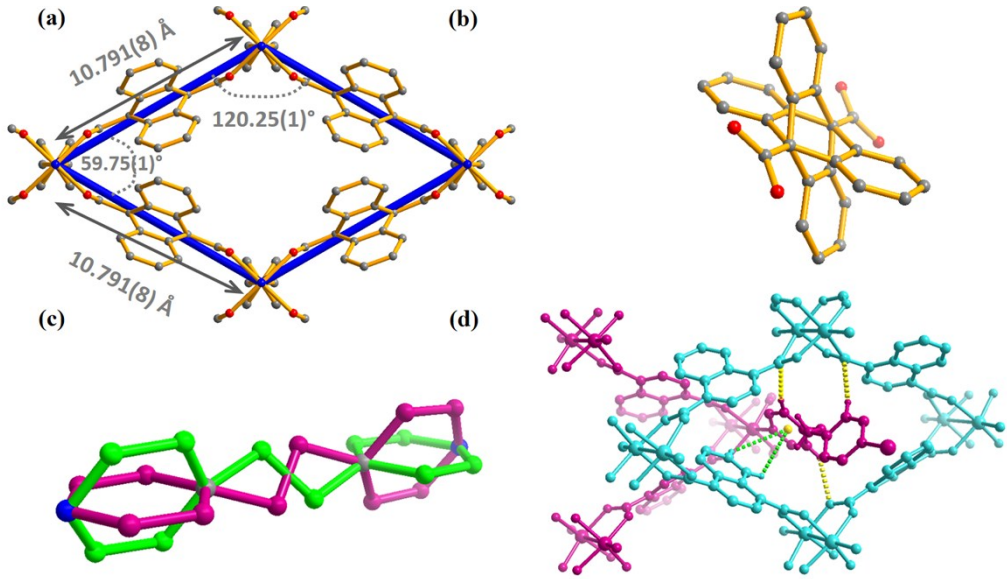

Fig. S2: (a) 2D net of $\mathbf{1}_{cp}$ with disordered naphthalene ring. (b) four-fold disordered naphthalene ring in ndc. (c) two disordered positions of bpa. (d) non-covalent interactions, C–H···O (yellow dotted lines) and C–H···π (green dotted lines) between the two nets of $\mathbf{1}_{cp}$. Hydrogen atoms are omitted and only one disordered orientation is shown for clarity.

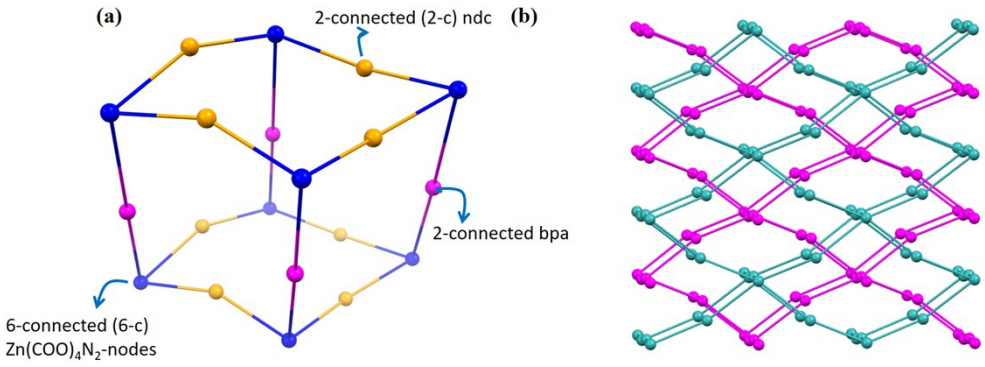

Fig. S3: (a) View of a single net of $\mathbf{1}_{cp}$. Examination with TOPOS[1] reveals that $\mathbf{1}_{cp}$ has a 2-nodal (2-c)3(6-c) periodic 3D net which is formed by 6-connected (6-c) $Zn(COO)_4N_2$-nodes and 2-connected (2-c) ndc and bpa linkers. The vertex symbol for the Zn-SBU, ndc, and bpa points are represented by Schläfli symbols, $\{8^{12}.12^3\}$, ^{2}, and ^{2}, respectively. (b) two-fold interpenetrated 3D nets of $\mathbf{1}_{cp}$. Further examination shows that $\mathbf{1}_{cp}$ adopts a topology with the Schläfli symbol $\{8^{12}.12^3\}^{23}$.

Thermogravimetric analysis (TGA)

Thermogravimetric analyses were carried out on a TA Instruments Q500 analyser. The instrument records weight loss as a function of temperature. Samples ranging in mass from 3 – 5 mg were placed in an aluminium pan and heated from room temperature to 600 °C at a rate of 10 °C min^{-1} under N_2 flow of 50 mL min^{-1}. Data analysis was carried out using the Universal Analysis 2000 (TA Instruments, Version 4.5A) software. The thermogravimetric analysis (TGA) of $\mathbf{1}_{cp}$ does not show any weight loss up to 350 °C and thereafter gradually decomposes into unidentified products (Fig. S4). The plateau in the TGA profile is due to the absence of any solvent molecule in the structure.

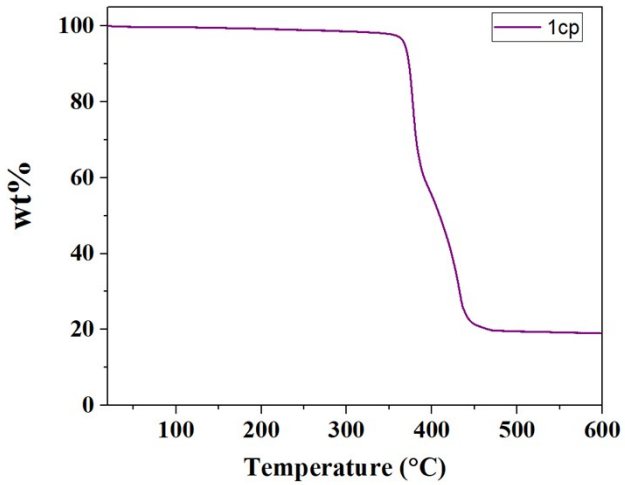

Fig S4: Thermogravimetric analysis of as-synthesised $\mathbf{1}_{cp}$.

Powder X-ray Diffraction (PXRD)

Experiments were carried out on a PANalytical X'Pert PRO instrument with Bragg–Brentano geometry. Intensity data were recorded using an X'Celerator detector, and 2θ scans in the range of 5–40° were performed with a step size of 0.02° at a scan speed of 0.02 °/s. During the experiment the powdered sample was exposed to $Cu_{K\alpha}$ radiation (λ = 1.5418 Å). $\mathbf{1_{cp}}$ was sealed within a glass capillary (environmental gas cell) and the capillary spinner configuration (with focusing mirror) of the instrument was used since this setup allows for very accurate temperature control using a short-nozzle Oxford Cryosystems Cryostream 700Plus cryostat. CO_2 gas was used to pressurise the sample, and its variable pressure PXRD patterns were measured at a constant temperature of 298 K. The PXRD pattern of the as-synthesized compound matches well with the simulated patterns obtained from single crystal X-ray diffraction data, suggesting phase purity of the as-synthesised compound (Fig. S5).

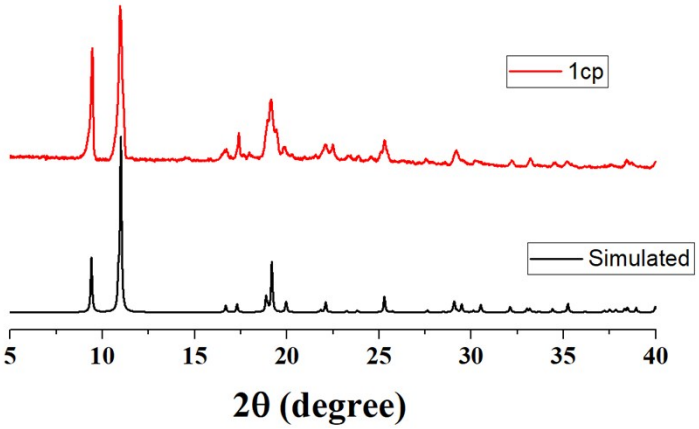

Fig S5: Simulated and experimental PXRD patterns of $\mathbf{1_{cp}}$ at 298 K.

Volumetric Sorption Analysis

A Setaram PCT Pro-E&E gas sorption analyser with a MicroDoser attachment was utilised to conduct high pressure gas sorption experiments with CO_2, CH_4 and N_2 (99.99% gas purity) at 298 K. The instrument utilises Sievert's volumetric method. The sample temperature was maintained to an accuracy of ±1 °C using a Grant refrigerated recirculation bath filled with antifreeze and water. A sample at known pressure and volume was connected to a reservoir of known volume and pressure through an isolation valve. The valve was opened, and the system allowed to equilibrate. The difference between the measured and calculated pressures was used to determine the amount of gas adsorbed. National Institute of Standards and Technology (NIST) software was used to calculate the thermodynamic corrections to account for the non-

ideal behaviour of the gases at relatively high pressures. Adsorbent samples weighing around 100-150 mg were placed in the sample tube and activated *in situ* under vacuum for 30 min. The dead volume of the sample cells was measured using helium gas with 99.99% purity. Blank runs for each gas were recorded to further correct for any other residual systematic errors in the experiment. Figure preparation and data analyses were performed using Microsoft Excel and OriginPro.

Pressure-Gradient Differential Scanning Calorimetry (PGDSC)

Experiments were carried out using a Setaram Micro-DSC7 Evo instrument. Heat flow was recorded at 298 K in the 1–52 bar pressure range of CO_2 gas. A freshly powdered sample of $\mathbf{1_{cp}}$ was used for each experiment. For a given sample weight, the energies involved for each event were calculated by integrating the peak area (heat flow in mW versus time in seconds) using Originpro version 8.0 software.

Single-crystal X-ray Diffraction

Single crystal X-ray diffraction data were collected on a Bruker D8 Venture diffractometer equipped with a PHOTON II CPAD detector and an Oxford Cryostream 800Plus cryostat. A multilayer monochromator with $Mo_{K\alpha}$ radiation (λ = 0.71073 Å) from an Incoatec $I_{\mu S}$ microsource was used. Data reduction was carried out by means of standard procedures using the Bruker software package SAINT[2] and absorption corrections and the correction of other systematic errors were performed using SADABS.[3] The structures were solved by direct methods using SHELXT[4] and refined using SHELXL-2018.3.[5] X-Seed[6] was used as the graphical interface for the SHELX program suite. Hydrogen atoms were placed in calculated positions using riding models. Squeeze analysis for $\mathbf{1_{lp}}$ using PLATON[7] shows 23.5 electrons per asymmetric unit (186 electrons per unit cell), which corresponds to one CO_2 molecule per asymmetric unit, or two CO_2 molecules per host formula unit. The occupancy of CO_2 molecules matches with the CO_2 sorption data at 50 bar.

In situ single-crystal X-ray diffraction

An in-house developed environmental gas cell was used to determine the crystal structures of the various phases at 298 K under controlled pressures. First, the structure of $\mathbf{1_{cp}}$ was

determined under reduced pressure (the capillary was evacuated prior to subsequent introduction of CO_2). The structure of $\mathbf{1}_{\mathbf{lp}}$ was determined after $\mathbf{1}_{\mathbf{cp}}$ was pressurised at 50 bar of CO_2. The crystal was not directly pressurised to 50 bar, instead it was pressurised at 5 bar increments and allowed to equilibrate for 1 hr at each point. Finally, after achieving 50 bar CO_2 pressure in the stepwise increase, the crystal was allowed to equilibrate for 12 hrs. The structure of $\mathbf{1}_{\mathbf{cp}}$ was determined after decreasing the pressure from 50 bar to 23 bar in the same stepwise manner. Note that pressurisation/depressurisation was carried out on a manifold and not while the crystal was mounted on the diffractometer; for this reason the crystal glued to the glass fibre inside the capillary may appear to have moved in between experiments, as shown in Fig. S16.

Table S1: Crystal data and structure refinement for $\mathbf{1_{cp}}$, $\mathbf{1_{lp}}$, $\mathbf{1_{np}}$ and $\mathbf{1_{cp}(des)}$

Identification code	$\mathbf{1_{cp}}$	$\mathbf{1_{lp}}$	$\mathbf{1_{np}}$	$\mathbf{1_{cp}(des)}$
Empirical formula	$C_{18}H_{10}NO_4Zn$	$C_{19}H_{12}NO_6Zn$	$C_{37}H_{24}N_2O_{10}Zn_2$	$C_{18}H_{10}NO_4Zn$
Formula weight	369.64	415.67	787.32	369.64
Temperature (K)	298(2)	300(2)	298(2)	298(2)
Wavelength (Å)	0.71073	0.71073	0.71073	0.71073
Crystal system	orthorhombic	monoclinic	monoclinic	orthorhombic
Space group	*Fmmm*	*C*2/*c*	$P2_1/m$	*Fmmm*
Unit cell dimensions (Å, °)	a = 10.7494(11) b = 16.2516(15) c = 18.7137(18) α = 90 β = 90 γ = 90	a = 16.556(8) b = 14.296(7) c = 16.325(8) α = 90 β = 97.679(12) γ = 90	a = 10.899(3) b = 16.264(5) c = 10.897(3) α = 90 β = 104.332(7) γ = 90	a = 10.7054(7) b = 16.2225(11) c = 18.7784(12) α = 90 β = 90 γ = 90
Volume (Å^3)	3269.2(5)	3829(3)	1871.5(9)	3261.2(4)
Z	8	8	2	8
Calculated density (g cm^{-3})	1.502	1.442	1.397	1.506
Absorption coefficient (mm^{-1})	1.523	1.316	1.338	1.527
F_{000}	1496	1688	800	1496
Crystal size (mm^3)	0.012 × 0.007 × 0.005	0.012 × 0.007 × 0.005	0.012 × 0.007 × 0.005	0.012 × 0.007 × 0.005
θ range for data collection (°)	2.519 to 25.370	2.176 to 25.003	2.300 to 25.454	2.169 to 26.500
Miller index ranges	$-12 \le h \le 12$, $-19 \le k \le 19$, $-22 \le l \le 22$	$-19 \le h \le 19$, $-15 \le k \le 16$, $-13 \le l \le 19$	$-13 \le h \le 10$, $-19 \le k \le 19$, $-10 \le l \le 13$	$-13 \le h \le 13$, $-20 \le k \le 20$, $-23 \le l \le 23$
Reflections collected	11630	14165	16299	19461
Independent reflections	852 [R_{int} = 0.0750]	3329 [R_{int} = 0.1154]	3589 [R_{int} = 0.0623]	956 [R_{int} = 0.0737]
Completeness to θ_{max} (%)	0.998	0.989	0.997	0.994
Data / restraints / parameters	852 / 30 / 73	3329 / 55 / 205	3589 / 66 / 366	956 / 36 / 82
Goodness-of-fit on F^2	1.076	1.032	1.033	1.060
Final R indices [$I > 2\sigma(I)$]	$R1$ = 0.0719, $wR2$ = 0.1782	$R1$ = 0.1048, $wR2$ = 0.2707	$R1$ = 0.0490, $wR2$ = 0.1220	$R1$ = 0.0713, $wR2$ = 0.1882
R indices (all data)	$R1$ = 0.0903, $wR2$ = 0.1945	$R1$ = 0.1820, $wR2$ = 0.3259	$R1$ = 0.0761, $wR2$ = 0.1395	$R1$ = 0.0931, $wR2$ = 0.2070
Largest diff. peak and hole (e Å^{-3})	0.871 and -1.696	1.677 and -1.044	0.696 and -0.794	0.984 and -1.022

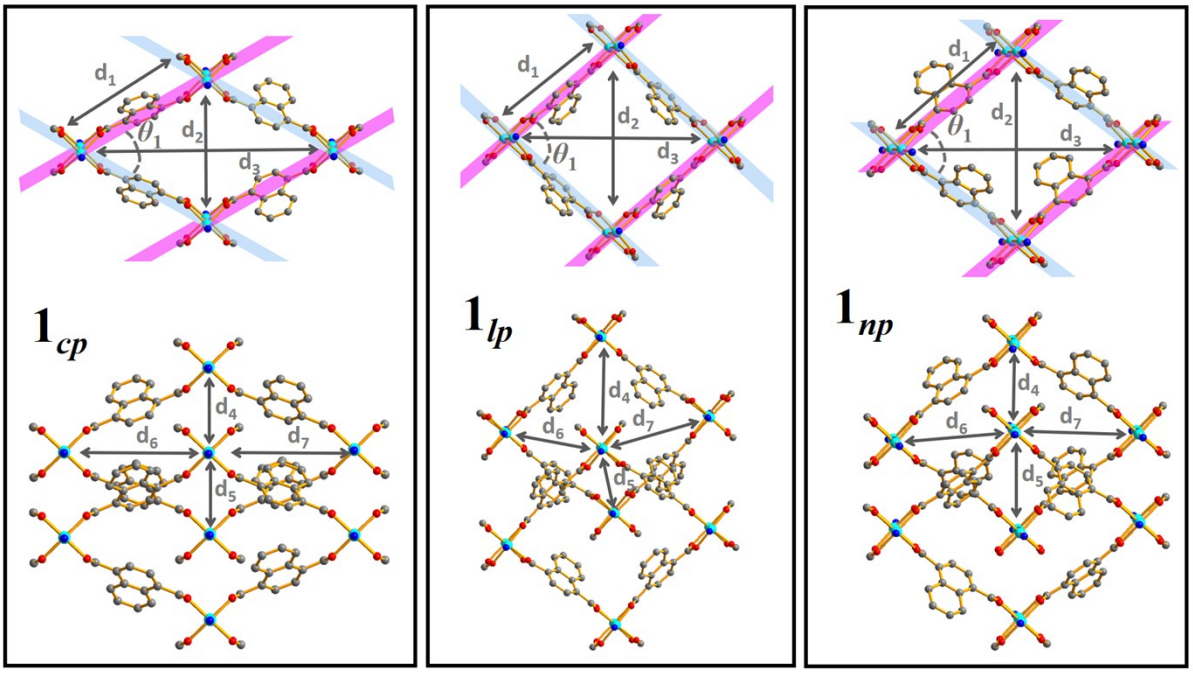

Fig. S6: Entangled nets position in $\mathbf{1}_{cp}$, $\mathbf{1}_{lp}$ and $\mathbf{1}_{np}$. Hydrogen atoms are omitted and only one disordered orientation is shown for clarity.

Table S2: Selected geometric measurements based on Figs. 6(b)-(d) and S6.

	d_1 (Å)	d_2 (Å)	d_3 (Å)	d_4 (Å)	d_5 (Å)	d_6 (Å)	d_7 (Å)	θ_1 (°)	θ_2 (°)
$\mathbf{1}_{cp}$	10.791(8)	10.743(1)	18.714(2)	9.743(7)	9.743(7)	12.393(8)	12.393(8)	59.747(8)°	30.424(8)
$\mathbf{1}_{lp}$	10.937(14)	14.296(7)	16.556(8)	11.847(4)	9.961(3)	10.916(3)	12.461(44)	81.621(7)°	28.553(16)
$\mathbf{1}_{np}$	10.899(3)	13.369(3)	13.369(2)	9.863(22)	11.293(8)	11.496(9)	12.306(22)	75.668(9)°	39.407(17)

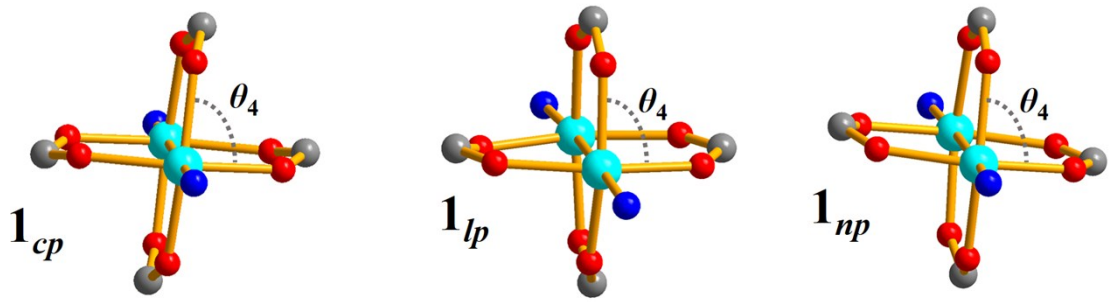

$\theta_4 = 87.28(11)°$ $\theta_4 = 89.74(15)°$ $\theta_4 = 89.28(16)°$

Fig. S7: The θ_4 angle as defined in this figure is largely maintained despite a dramatic change in net angle and inter-net distance due to the hinge-motion during the phase transformations.

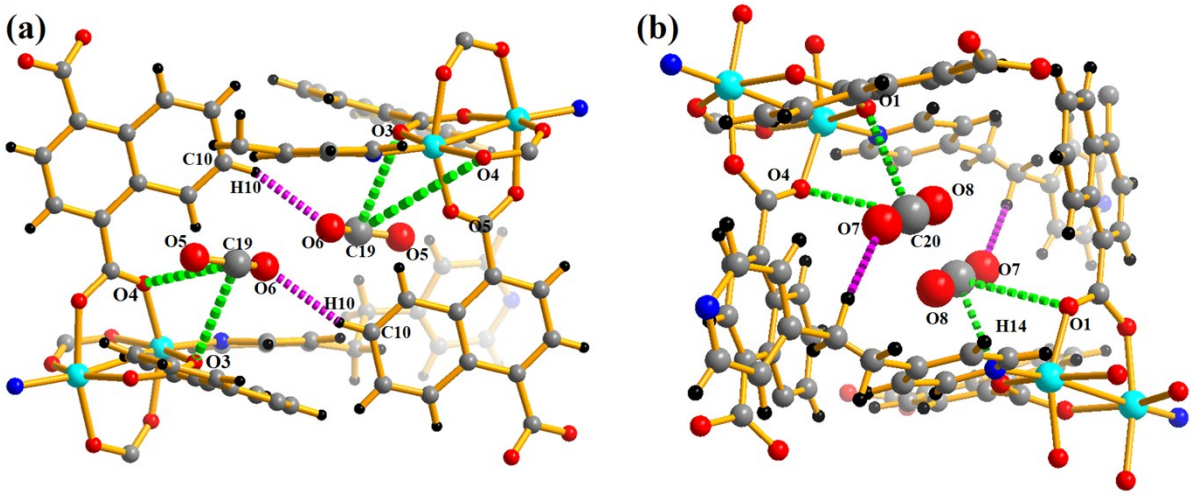

Fig. S8: Perspective view showing the interaction of host $\mathbf{1_{lp}}$ with guest CO_2 molecules (a) type A and (b) type B. Green dotted lines represents the interaction between the carbon atoms of the guest CO_2 and the oxygen atoms of the carboxylate groups while the pink dotted lines represent the C–H···O interactions.

Table S3: Non-bonding interactions in $\mathbf{1_{lp}}$ described in Fig. S8 from SCD data.

		D···A	**Distance (Å)**	**D-H···A**	**angle (°)**
$\mathbf{1_{lp}}$	***Type A***	C10···O6	3.517(24)	C10-H10···O6	160.17(14)
		Carboxylate···CO_2 interaction (Å)		C19···O3	3.465(9)
				C19···O4	3.878(10)
	Type B	C18···O7	3.881(3)	C18-H18B···O7	143.90(18)
		Carboxylate···CO_2 interaction (Å)		C20···O4	3.632(11)
				C20···O1	3.187(9)

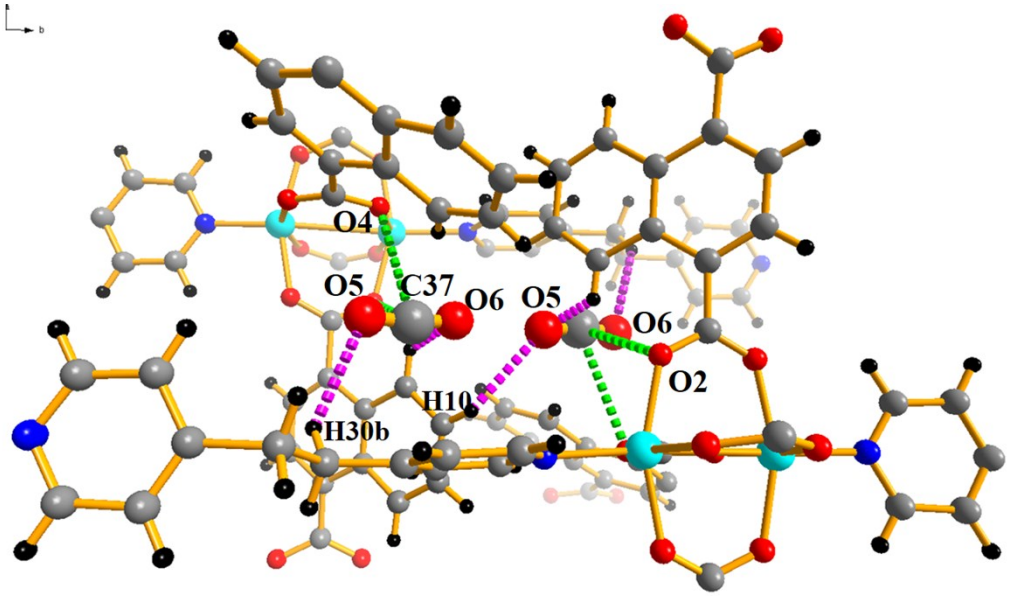

Fig. S9: Perspective view showing the interaction of host $\mathbf{1_{np}}$ with guest CO_2 molecules. Green dotted lines represents the interaction between the carbon atoms of the guest CO_2 and the oxygen atoms of the carboxylate groups while the pink dotted lines represents the C–H···O interaction.

Table S4: Non-bonding interactions in $\mathbf{1_{np}}$ described in Fig. S9 from SCD data.

	D···A	**Distance (Å)**	**D-H···A**	**angle (°)**
$\mathbf{1_{np}}$	C10···O5	3.329(7)	C10-H10···O5	130.70(12)
	C11···O5	2.132(9)	C11-H11···O5	125.21(10)
	C30···O6	3.545(9)	C30-H30···O5	135.05(10)
	Carboxylate···CO_2 interaction (Å)		C37···O2	3.283(6)
			C37···O4	3.307(7)

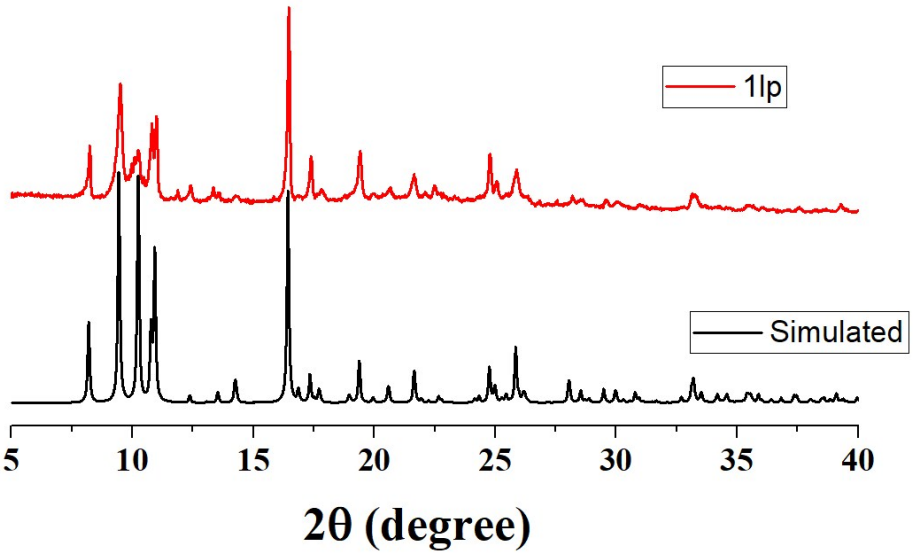

Fig. S10: Simulated and experimental PXRD patterns of $\mathbf{1_{lp}}$ at 298 K.

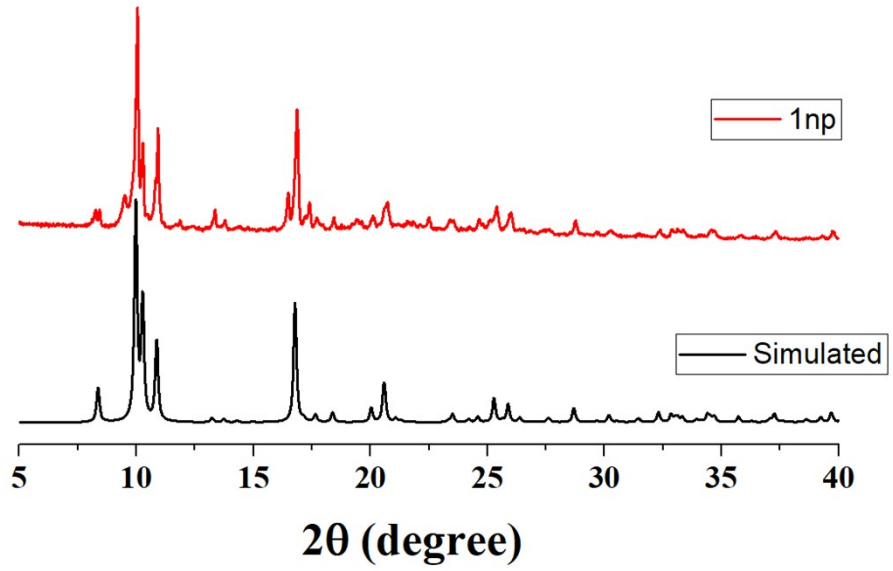

Fig. S11: Simulated and experimental PXRD patterns of $\mathbf{1_{np}}$ at 298 K.

Computational Details

(a) DFT calculations

In order to gain insight regarding the CO_2 adsorption nature for the two types of CO_2 dimers adsorbed inside the MOF $\mathbf{1_{lp}}$, we have used periodic density functional theory (periodic-DFT) based calculations. The optimal location of CO_2 molecules inside 1 x 1 x 1 cell of $\mathbf{1_{lp}}$ and $\mathbf{1_{np}}$ were determined using the QUICKSTEP module implemented in the CP2K 6.1 software package.[8] The valence electrons have been treated in a mixed basis set with an energy cutoff of 300 Ry and using molecularly optimised double-zeta single polarisation (DZVP) short range basis. The effect of core electrons and nuclei was considered by using norm-conserving pseudopotentials of Goedecker-Teter-Hutter (GTH).[9] The Perdew-Burke-Ernzerhof (PBE)[10] functional was used for electron exchange and correlation interactions and Grimme's DFT-D3 empirical van der Waals terms[11] were added to account for dispersion interactions. The atomic positions were optimised such that each component of force was less than 10^{-4} a.u. The DFT optimised geometry and cell parameters for $\mathbf{1_{lp}}$ and $\mathbf{1_{np}}$ with the disorder removed are summarised in Table S5. There is only ~2.2% maximum volume change with respect to the experimental cell parameters, which confirms the reliability of the DFT calculation.

Table S5: Optimised unit cell parameters of $\mathbf{1_{np}}$ and $\mathbf{1_{lp}}$ and percentage of error in volume with respect to experimental volume. Cell angles kept constant for $\mathbf{1_{np}}$ during optimisation.

Pressure	System	a (Å)	b (Å)	c (Å)	α (°)	β (°)	γ (°)	V (Å^3)	ΔV (%)
$\mathbf{1_{np}}$	Experiment	10.899	16.264	10.897	90.00	104.33	90.00	1871.5	-
	Empty Framework	10.989	16.300	11.023	90.00	104.33	90.00	1913.0	-2.22
	Framework with CO_2	10.976	16.272	10.984	90.00	104.33	90.00	1900.855	-1.57
$\mathbf{1_{lp}}$	Experiment	16.556	14.296	16.325	90.00	97.68	90.00	3829.2	-
	Empty Framework	16.996	14.075	16.253	90.00	96.70	90.00	3861.5	-0.84
	Framework with CO_2	16.975	14.052	16.239	90.01	96.55	89.96	3848.19	-0.49

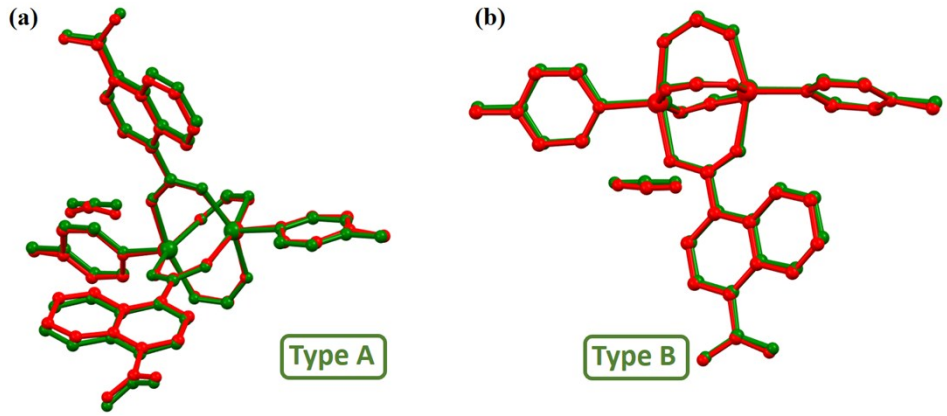

Fig S12: Overlay of the experimental (red) and geometry optimised (green) structures of $\mathbf{1}_{lp}$ type A (a) and type B (b) CO_2 position showing negligible deviations.

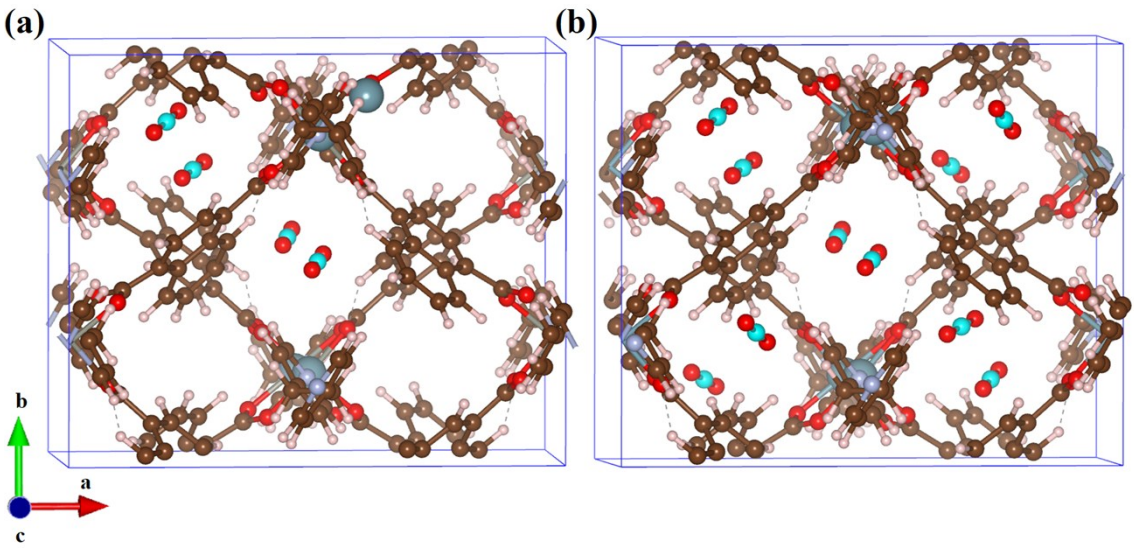

Fig. S13: Optimised structure of (a) positions of the two types of CO_2 molecules and (b) the fully loaded $\mathbf{1}_{lp}$, viewed along [001]. Colour code: brown – MOF carbon, red – oxygen, pink – hydrogen, dark cyan – zinc, ice blue – nitrogen, cyan – CO_2 carbon.

The binding energy (BE) for CO_2 was calculated with and without correcting the Basis Set Superposition Error (BSSE) using the counterpoise method[12] according to the following equation:

$$\Delta E = E(MOF + CO_2) - E(MOF) - nE(CO_2)$$

Here, ΔE, $E(MOF + CO_2)$, $E(MOF)$ and $E(CO_2)$ are the BE, energies of the MOF with adsorbed CO_2, energy of the MOF and energy of an isolated CO_2 molecule, respectively. The energy of the isolated CO_2 molecule was calculated in the same simulation box size as that of the MOF. All the structures were visualised with Mercury,[13] VMD,[14] Vesta[15] and BIOVIA Materials Studio[16] packages.

Table S6: Tabulated results for host-guest Binding Energy and BSSE corrected Binding Energy per CO_2 molecule in kJ mol^{-1} [n = 2 for type A and B CO_2 dimers; n = 4 for Type A and B combined]

MOF	BE (framework + Type A CO_2)	BE (framework + Type B CO_2)	BE (framework + Type A and B CO_2)	BSSE corrected BE (framework + Type A CO_2)	BSSE corrected BE (framework + Type B CO_2)	BSSE corrected BE (framework + Type A and B CO_2)
$\mathbf{1_{lp}}$	-45.181	-40.219	-41.718	-40.090	-34.348	-38.513
	BE (framework + CO_2)			BSSE Corrected BE (framework + CO_2)		
$\mathbf{1_{np}}$	-47.902			-40.672		

The electron density difference maps (EDDMs) were plotted to account for the nature of interactions that CO_2 encounters with the carboxylate and aromatic C–H of the linker groups, and it was calculated using the relation:

$$\Delta\rho = \rho(MOF + CO_2) - \rho(MOF) - \rho(CO_2)$$

where, $\Delta\rho$ is the electron density difference and $\rho(MOF + CO_2), \rho(MOF), \rho(CO_2)$ are the electron densities for the total system and individual MOF and CO_2, respectively. The plots are shown in Fig. S14. We can clearly see the interaction between the carboxylate group of the paddlewheel SBU, as well as the C–H of the linker with the Type A and B CO_2 molecules in $\mathbf{1_{lp}}$ from the density maps. In case of $\mathbf{1_{np}}$, the $\mathbf{CO_2}$ molecules are farther apart (~8 Å) with negligible guest-guest interaction but the π-cloud of the CO_2 interacts very strongly with the CH_2–CH_2 group and the carboxylate unit, thereby rationalizing the fact why it remains bound to the framework up to 23 bar during desorption (Table S6).

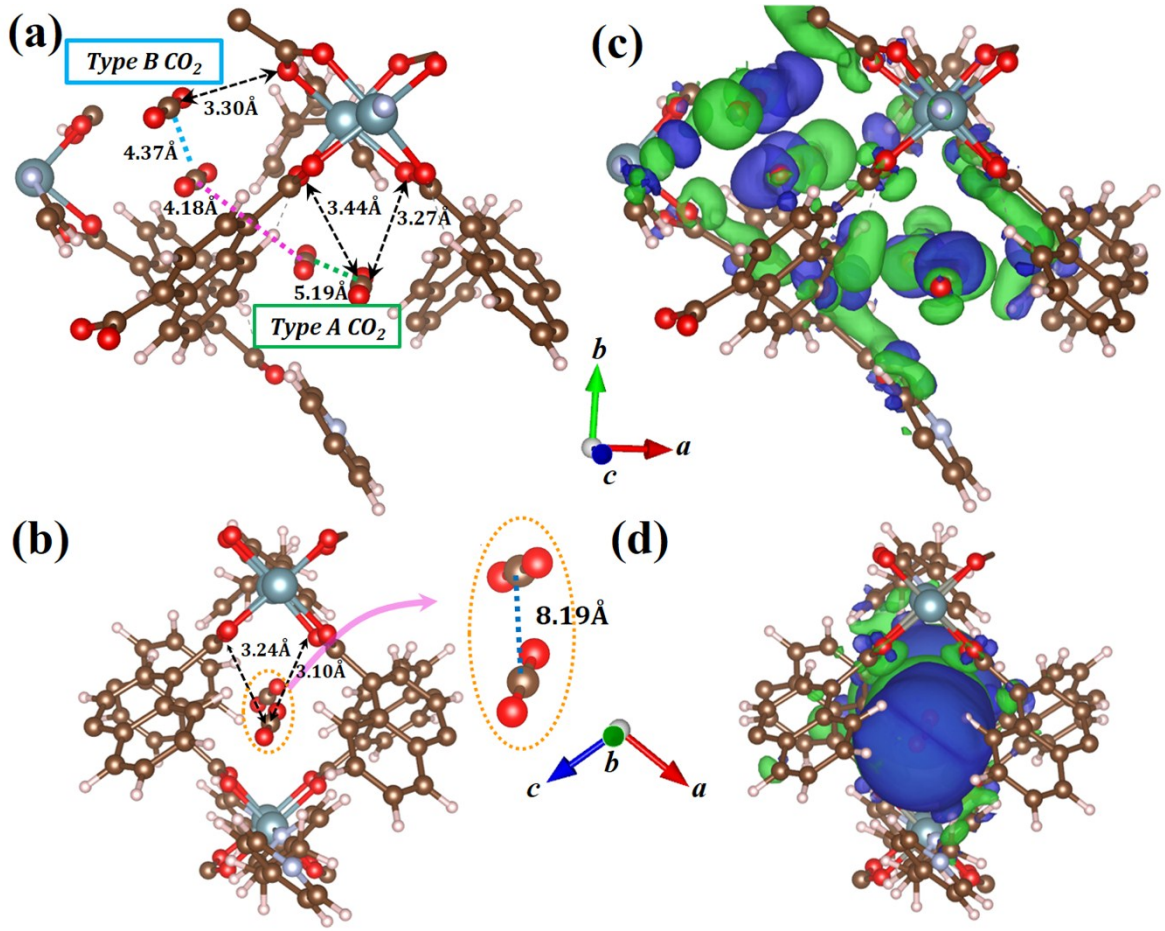

Fig. S14: (a) Type A and B CO_2 positions inside the geometry optimised structure of $\mathbf{1_{lp}}$; Guest-guest interactions between two Type A, two Type B and between a Type A-B CO_2 dimer are shown as pink, green and blue dashed lines, respectively. (b) CO_2 positions inside the geometry optimised structure of $\mathbf{1_{np}}$; (c) and (d) areas of the EDDMs with increased (green) and decreased (blue) electron densities with respect to the isolated MOF and CO_2 molecules for $\mathbf{1_{lp}}$ and $\mathbf{1_{np}}$, respectively. The isosurface value is 0.0003 a.u. Colour code: brown –carbon, red – oxygen, pink – hydrogen, dark cyan – zinc, ice blue – nitrogen, cyan – CO_2 carbon. The EDDMs were calculated for the entire MOF + CO_2 system and only a small section is shown for clarity.

(b) GCMC simulations

Owing to positional disorder, periodic models were geometry optimised using the CASTEP[17] code implemented in Materials Studio[16] with atoms initially in their crystallographic positions. The density functional theory (DFT) generalised gradient approximation of Perdew-Burke-Ernzerhof (PBE)[10a] in combination with Grimme's DFT-D dispersion correction[11a] was employed with on-the-fly generated Vanderbilt-type ultrasoft pseudopotentials[18] in combination with the Koelling-Harmon scalar-relativistic approach[19] and a planewave expansion to an energy cutoff of 489.8 eV. Integration in the reciprocal lattice was performed using a Monkhorst-Pack grid[20] with a 0.05 $Å^{-1}$ k-point separation and self-consistent field convergence was set to 2.0×10^{-6} eV. A 50% admixture of the charge density[21] was applied in conjunction with a DIIS (direct inversion in an iterative subspace)[22] size of 20 to speed up convergence. Convergence tolerances for geometry optimization using the BFGS (Broyden-Fletcher-Goldfarb-Shanno) algorithm[23] were set to 2.0×10^{-5} eV $atom^{-1}$, 0.05 eV $Å^{-1}$ and 2.0×10^{-3} Å on energy, maximum force and maximum displacement, respectively.

Grand-canonical Monte Carlo (GCMC) simulations were carried out at 298 K to simulate adsorption isotherms. In this ensemble, adsorbate chemical potential μ, volume V and temperature T are held fixed while the number of adsorbate molecules in the framework is allowed to fluctuate. Simulations were performed at 298 K using the Sorption Metropolis Monte Carlo module[24] of Materials Studio employing Lennard-Jones parameters from the DREIDING force field.[25] Hirshfeld charges[26] were derived from the periodic-DFT geometry optimizations. Atom-based summation was applied for van der Waals interactions to a cut-off distance of 18.5 Å using cubic spline truncation. Electrostatic interactions were handled using the Ewald summation technique with a precision of 1.0×10^{-5} kcal mol^{-1}.[27]

The geometry optimized $\mathbf{1_{np}}$ and $\mathbf{1_{lp}}$ frameworks were kept rigid during simulations with CO_2 as sorbate up to 50 bar. The simulation box consisted of one unit cell with periodic boundary conditions applied in all three dimensions. Simulations were carried out with 1×10^6 equilibration and 1×10^7 production steps,[24] where each step attempts to translate, rotate, insert, remove or relocate an adsorbate molecule with equal probability.

The simulated total uptake was converted to excess uptake for comparison to experimental results. The bulk density, $\rho_{bulk}(T,P)$, and pore volume of the framework, V_{pore}, is used to calculate the amount of CO_2 that would be present in the pores of the framework without any adsorption taking place; that is, in the absence of any host-guest interactions.

$$N_{excess} = N_{total} - N_{bulk}$$

where

$$N_{bulk} = \rho_{bulk}(T,P)V_{pore}$$

The bulk density of CO_2 was obtained from NIST.[28] The pore volume was determined using the *Atoms Volume & Surfaces* tool of the Materials Studio Visualizer employing a 1.6 Å probe radius as 980.22 and 174.83 Å^3 for $\mathbf{1}_{\mathbf{lp}}$ and $\mathbf{1}_{\mathbf{np}}$, respectively.

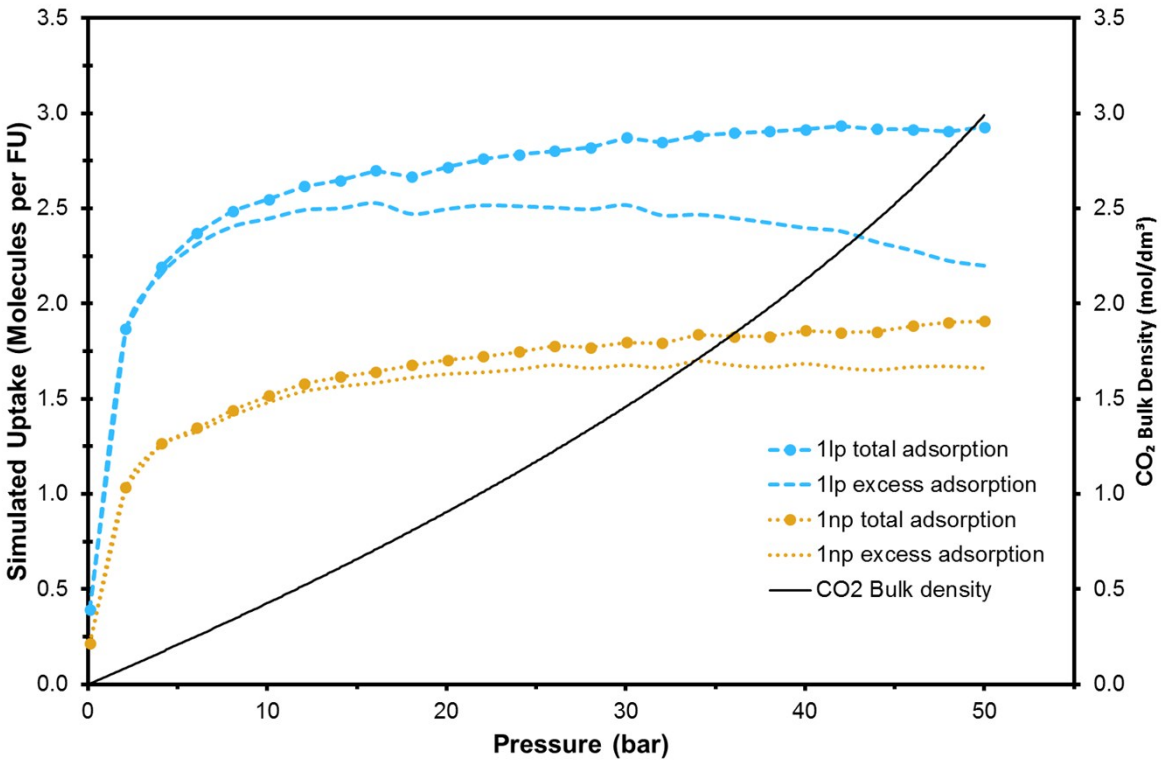

Fig. S15: Comparison of simulated total and excess adsorption results.

Diffraction frames

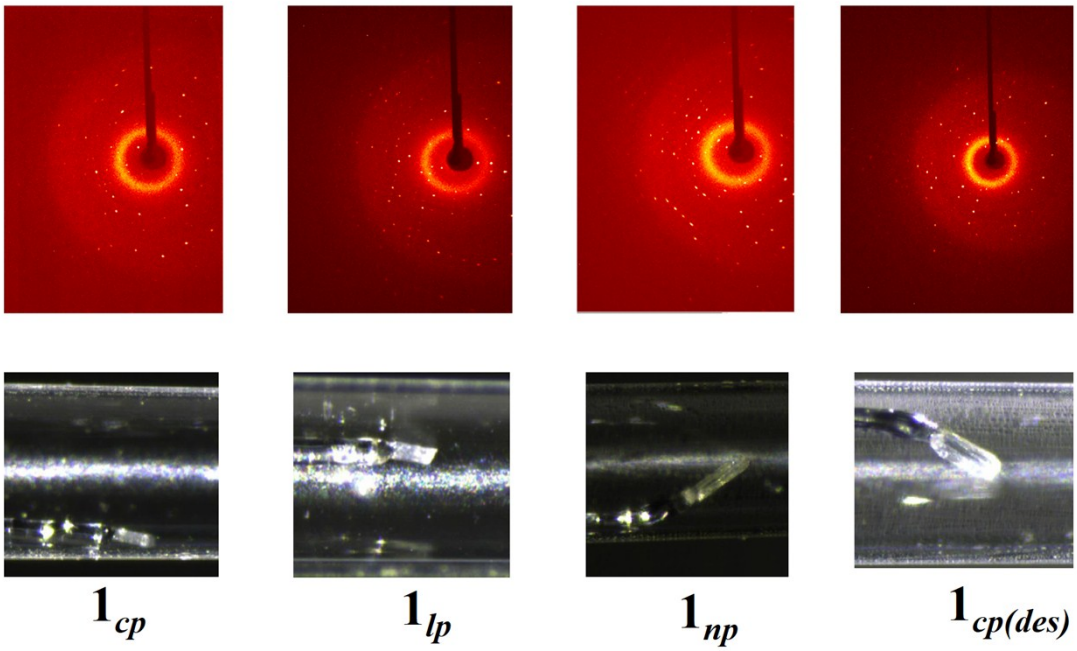

Fig. S16: Selected frames showing X-ray diffraction patterns for $\mathbf{1}_{cp}$, $\mathbf{1}_{lp}$, $\mathbf{1}_{np}$ and $\mathbf{1}_{cp(des)}$ at 298 K. Also shown are photographs of the same crystal centred in the X-ray beam following equilibration at reduced pressure ($\mathbf{1}_{cp}$), 52 bar ($\mathbf{1}_{lp}$), 23 bar ($\mathbf{1}_{np}$) and atmospheric ($\mathbf{1}_{cp(des)}$) CO_2 gas pressure. As mentioned above, apparent movement of the crystal is owing to unmounting and remounting the same crystal glued inside the gas cell.

Supporting information references:

1. (a) V. A. Blatov, A. P. Shevchenko and V. N. Serezhkin, *J. Appl. Crystallogr.*, 2000, **33**, 1193; (b) V. A. Blatov, L. Carlucci, G. Ciani and D. M. Proserpio, *CrystEngComm*, 2004, **6**, 377.
2.S. V. a. SMART (V 5.628), XPREP, SHELXTL; Bruker AXS Inc. Madison, Wisconsin, USA, 2004.
3.G. M. Sheldrick, *SADABS, Empirical Absorption Correction Program, University of Göttingen, Göttingen*, 1997.
4.G. M. Sheldrick, *Acta Crystallographica Section A*, 2015, **71**, 3.
5.G. M. Sheldrick, *Acta Crystallographica Section C*, 2015, **71**, 3.
6.L. J. Barbour, *Journal of Supramolecular Chemistry*, 2001, **1**, 189.
7.A. Spek, *J. Appl. Crystallogr.*, 2003, **36**, 7.
8.J. VandeVondele, M. Krack, F. Mohamed, M. Parrinello, T. Chassaing and J. Hutter, *Computer Physics Communications*, 2005, **167**, 103.
9.M. Elstner, D. Porezag, G. Jungnickel, J. Elsner, M. Haugk, T. Frauenheim, S. Suhai and G. Seifert, *Physical Review B*, 1998, **58**, 7260.
10. (a) J. P. Perdew, K. Burke and M. Ernzerhof, *Phys. Rev. Lett.*, 1996, **77**, 3865; (b) J. P. Perdew, A. Ruzsinszky, G. I. Csonka, O. A. Vydrov, G. E. Scuseria, L. A. Constantin, X. Zhou and K. Burke, *Physical Review Letters*, 2008, **100**, 136406; (c) Y. Zhang and W. Yang, *Physical Review Letters*, 1998, **80**, 890.
11. (a) S. Grimme, *J. Comput. Chem.*, 2006, **27**, 1787; (b) S. Grimme, J. Antony, S. Ehrlich and H. Krieg, *J. Chem. Phys.*, 2010, **132**, 154104.
12. (a) H. B. Jansen and P. Ros, *Chem. Phys. Lett.*, 1969, **3**, 140; (b) B. Liu and A. D. McLean, *The Journal of Chemical Physics*, 1973, **59**, 4557.
13.C. F. Macrae, I. J. Bruno, J. A. Chisholm, P. R. Edgington, P. McCabe, E. Pidcock, L. Rodriguez-Monge, R. Taylor, J. van de Streek and P. A. Wood, *Journal of Applied Crystallography*, 2008, **41**, 466.
14.W. Humphrey, A. Dalke and K. Schulten, *Journal of Molecular Graphics*, 1996, **14**, 33.

15.K. Momma and F. Izumi, *Journal of Applied Crystallography*, 2011, **44**, 1272.
16.*Dassault Systèmes BIOVIA, Materials Studio*, 2017, Release 18.
17.J. Clark Stewart, D. Segall Matthew, J. Pickard Chris, J. Hasnip Phil, I. J. Probert Matt, K. Refson and C. Payne Mike, in *Zeitschrift für Kristallographie - Crystalline Materials*, 2005, p. 567.
18.D. Vanderbilt, *Physical Review B*, 1990, **41**, 7892.
19.D. D. Koelling and B. N. Harmon, *Journal of Physics C: Solid State Physics*, 1977, **10**, 3107.
20.H. J. Monkhorst and J. D. Pack, *Physical Review B*, 1976, **13**, 5188.
21.G. Kresse and J. Furthmüller, *Physical Review B*, 1996, **54**, 11169.
22.P. Pulay, *Chem. Phys. Lett.*, 1980, **73**, 393.
23.B. G. Pfrommer, M. Côté, S. G. Louie and M. L. Cohen, *Journal of Computational Physics*, 1997, **131**, 233.
24.N. Metropolis, A. W. Rosenbluth, M. N. Rosenbluth, A. H. Teller and E. Teller, *J. Chem. Phys.*, 1953, **21**, 1087.
25.S. L. Mayo, B. D. Olafson and W. A. Goddard, *The Journal of Physical Chemistry*, 1990, **94**, 8897.
26.F. L. Hirshfeld, *Theoretica chimica acta*, 1977, **44**, 129.
27.P. P. Ewald, *Annalen der Physik*, 1921, **369**, 253.
28.*Thermophysical Properties of Fluid Systems" by Eric W. Lemmon, Mark O. McLinden and Daniel G. Friend in NIST Chemistry WebBook, NIST Standard Reference Database Number 69, Eds. P.J. Linstrom and W.G. Mallard, National Institute of Standards and Technology, Gaithersburg MD, 20899.*